
# UNIVERSITÀ DEGLI STUDI DI PADOVA

**Dipartimento di Fisica e Astronomia "Galileo Galilei"**

**Corso di Laurea in Fisica**


**Tesi di Laurea**

## Progettazione e fabbricazione di ottiche diffrattive 3D mediante litografia ottica maskless

## Design and fabrication of 3D diffractive optics via maskless optical lithography


**Relatore**

**Dr. Gianluca Ruffato**

**Laureando**

**Tommaso Pirazzo**


**Anno Accademico 2023/2024**

**Abstract**

In front of the impelling need for integrated and miniaturized technological devices, diffractive optics represent an effective solution in order to replace standard bulk optical elements with their almost flat counterparts. Furthermore, the diffractive-optics paradigm enables the integration of multiple operations into the same optical element, opening to the complex spatial manipulation of light in many research and technological fields. In this thesis, we optimize a lithographic protocol for the fabrication of 3D diffractive optics using maskless optical lithography. The performed laboratory activities can be divided into two main parts: the realization of simple optical elements, and their morphological and optical characterizations. The technique offers a fast, versatile, and effective solution for the fabrication of surface relief structures with micrometric resolution. Several optical designs are considered for applications in the visible range, such as blazed gratings and Fresnel lenses.

Di fronte all'urgente richiesta di dispositivi elettronici e miniaturizzati, le ottiche diffrattive offrono una soluzione efficace per la sostituzione di elementi ottici standard spessi con equivalenti decisamente più sottili. Inoltre, il modello delle ottiche diffrattive permette l'integrazione di più funzioni nello stesso elemento ottico, aprendo alla manipolazione spaziale della luce in molti campi tecnologici e di ricerca. In questo elaborato, si ottimizza una procedura litografica per la fabbricazione di ottiche diffrattive 3D con l'uso della litografia ottica maskless. L'attività di laboratorio svolta può essere divisa in due parti principali: la realizzazione di semplici elementi ottici, e la loro caratterizzazione ottica e morfologica. La tecnica impiegata offre una soluzione veloce, versatile ed efficace per la realizzazione di strutture a rilievi superficiali di risoluzione micrometrica. Sono stati considerati diversi disegni ottici per applicazioni nello spettro del visibile, come per esempio reticoli di diffrazione e lenti di Fresnel.

# Contents

**Introduction** **vii**

**1 Process for the fabrication of three-dimensional diffractive optics** **1**
1.1 What's a three-dimensional diffractive optical element ? . . . 1
1.2 Grayscale maskless lithography . . . 1
1.3 Experimental procedure and instruments . . . 2
1.3.1 Optical elements fabrication . . . 4
1.3.2 Optical characterization . . . 6

**2 Dose Calibration** **9**
2.1 Dose Matrix design and fabrication . . . 9
2.2 Data analysis . . . 10
2.2.1 Dose curves . . . 10
2.2.2 Remarks on n-over technique and post-baking . . . 14
2.3 Results . . . 14

**3 Blazed grating** **15**
3.1 Design and fabrication . . . 15
3.1.1 Expected behavior of the system . . . 15
3.1.2 Fabrication parameters definition . . . 16
3.2 Data analysis . . . 16
3.2.1 Profile measurement . . . 16
3.2.2 Testing on optical bench . . . 17
3.3 Results . . . 19

**4 Fresnel lenses** **21**
4.1 Design and fabrication . . . 21
4.1.1 Expected behavior of the system . . . 21
4.1.2 Fabrication parameters definition . . . 22
4.2 Data analysis . . . 22
4.2.1 Profile measurement . . . 22
4.2.2 Testing on optical bench . . . 23
4.3 Results . . . 24

**5 Conclusions** **25**

**Bibliography** **27**

# Introduction

The main purpose of this work is the design and fabrication of three-dimensional diffractive optics using maskless optical lithography. In this work we will explain all the subsequent steps for the creation of two different types of optical elements starting from the scratch up to the testing of their behavior on the optical bench. First stage in this process was the training and calibration of the $\mu$MLA [1]. After that, we made samples of blazed gratings and Fresnel lenses based on the theory of Fourier Optics. Initially the realized samples were tested on the profilometer and then on the optical bench to observe their real effects on a monochromatic light beam in the far field. Production of optical elements such as blazed gratings, lenses or holograms is not a new feature in optics and photonics. We are already able to produce good quality optics with, for example, the EBL [2] technique. In particular, the main aspect of this work is the use of a maskless lithography technique in the realization of diffractive optical elements (DOE). This method offers a more versatile, simple to use and faster technique then the "masked" lithography. In fact, adopting maskless lythography, we are able to obtain a relatively smooth 3D surface with a single exposure. To achieve a similar result using masks we had to produce a lot of different masks and repeat the exposure procedure several times. In fact, for each step we are able to produce only a binary pattern layer. Another problematic aspect is that the replacing masks procedure causes alignment errors. All those characteristics of masked lithography represents an evident limit for the realization of complex 3D structures. In the maskless optical lithography we can produce complex 3D structures on very thin photoresist's layers with a single exposure procedure lasting a few minutes. The chapters are organized as follows:

- In chapter 1 we will give a general overview of the adopted process for the fabrication of three-dimensional DOEs. We will start introducing shortly the main idea on the working principle of DOEs and we will describe the maskless lithography technique and the experimental procedure.
- In chapter 2 we will present the followed process to obtain the correct values of dose and to observe the linear response of the selected photoresist for the optical maskless lithography.
- In chapter 3 we will describe the design, fabrication and testing procedure of blazed gratings.
- In a similar way of chapter 3, in chapter 4 we will describe the design, fabrication and testing procedure of Fresnel lenses.

[1] Machine for the optical lithography of samples. This is the main process of the maskless lithography that we will discuss in the follow

[2] Electron beam lithography.

# Chapter 1

# Process for the fabrication of three-dimensional diffractive optics

## 1.1 What's a three-dimensional diffractive optical element ?

The most common optical elements such as, for example, spherical lenses, have the problem to require too much volume. So they are not suitable to satisfy the technological requirement of miniaturization. Actually, this problem is not a new one. In fact, the first scientist to find out a solution to reduce the manufacturing material for huge spherical lenses adopted in the lighthouses has been Augustine-Jean Fresnel in 1827. He observed that it was possible to focus light beam also removing all the bulk material of a lens. To export the unnecessary material he thought to "slice" the lens along perpendicular direction to the optical axis with a spatial frequency corresponding to a phase shift of the traveling wave that didn't change the focusing effect of the lens. The phase pattern of the transmitted wave across the DOE is caused by the point by point variation of the optical path length. The material that completely fills the volume of the "slices" can be removed since in this region is not introduced variations of optical path length. Considering the DOE's material refractive index $n$, if the surrounding medium is air, the phase pattern of the transmitted wave is given by the expression[1]:

$$\Delta\phi(x,y) = \frac{2\pi}{\lambda}(n - n_{air})d(x,y) \quad \Rightarrow \quad d_{max} = \frac{\lambda}{n-1} \tag{1.1}$$

where $\lambda$ is the wavelength, $d(x,y)$ is the medium thickness and $d_{max}$ is the maximum medium thickness to obtain $\Delta\phi = 2\pi$.

The focusing effect is caused by the profile shape and is not affected by the material in the bulk. So, the only part of the lens that we need is the one at the interface between the two media. This simple example explain the main idea of optical lithography: realize three-dimensional diffractive elements whose optical fuctionality is based on its own surface reliefs. These structures are able to cause a spatially-variant phase shifting and so produce the desired optical effect saving up a lot of volume and material. Furthermore, applying the tools of the Fourier Optics and the Kirchhoff diffraction theory, we are able to engineer surface shapes to produce the desired effect. Optical elements could be designed to work with transmitted or reflected light beams.

## 1.2 Grayscale maskless lithography

Optical lithography is a particular technique to realize very thin structures on plane surfaces. The requested thickness of these three-dimensional optical elements is given by the expression (1.1). Assuming $\lambda \simeq 630\ nm$ [2] and refracting index of the material adopted to realize the optical element

[1] We are assuming that the incident wave is a plane monochromatic wave.

[2] Red light wavelength

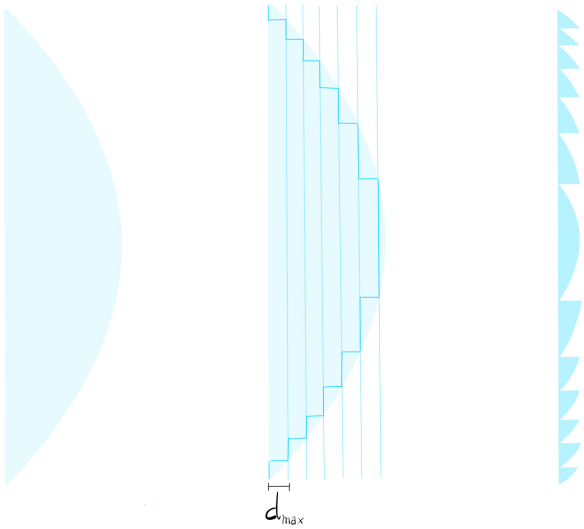


Figure 1.1: example of how to obtain the thin equivalent version of a spherical lens from the classical one.

$n \simeq 1.5$, we find $d_{max} \simeq 1260\ nm$. In particular, maskless optical lithography techniques consists in exposing to a UV source a thin layer of photosensitive material without any kind of mask. The intensity pattern to realize the desired structure is directly modulated after the UV source. After the exposure to UV light, the photosensitive material changes its solubility index proportionally to the UV intensity beam. In case of positive resist[3], after development the exposed material is removed to obtain the desired three-dimensional structure. Absence of a mask is one of main differences between this technique and other lithography methods. Since we had to realize transmission optics we adopted transparent glass substrates. Then, the photosensitive layer to expose was deposited above.

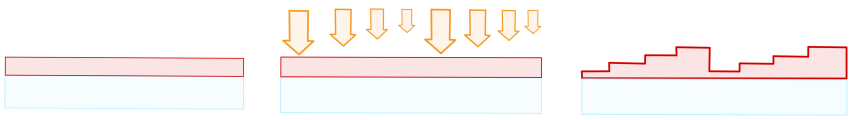

Figure 1.2: the three main step of mask-less lithography: photoresist coating, exposure, development of the final structure.

The pattern of desired surface structure, that is the depth of the resulting layer point by point, is encoded in a 8-bit grayscale image. Each gray level between 0 and 255 corresponds to a UV dose value and therefore to a precise depth. In this way we were able to calibrate the laser writer[4] to realize the desired pattern on the sample's surface. So, before starting to realize our optical elements, we needed to investigate the dose range for the desired photoresist linear response interval. In this way we were able to correlate the film thickness with the released dose. This aspect will be presented in chapter 2.

## 1.3 Experimental procedure and instruments

In this section we will present the instruments and the general procedure adopted for all the samples realized. All the following instruments and materials are located in the clean room of Department of Physics and Astronomy. In the same laboratories all the steps of the sample production and their morphological characterization were carried out. The optical bench adopted for the DOE optical characterization is located in another structure near the DFA.

[3]We will present the main difference between positive and negative photoresist in the paragraph 1.3.
[4]Machine to expose the prepared samples.

### The $\mu MLA$ laser writer

The $\mu MLA$ is the laser writer machine adopted to perform maskless optical lithography in this work. The $\mu MLA$ is assembled by Heidelberg Instruments Mikrotechnik GmbH [6]. The machine is connected to a dedicated PC where a special software for its control is installed. In $\mu MLA$ the pattern saved in a 8-bit grayscale bitmap file is directly exposed on the photoresist layer. There are two different way to perform the exposure: the raster scan mode and the vector scan mode. We adopted the first exposure mode. To work in this mode the $\mu MLA$ uses a digital micro-mirror device (DMD) to shape the UV source and expose a spatially structured intensity zone. In this mode the $\mu MLA$ has 2 different light source available [5]. For this work we adopted as light source the led with $\lambda = 365\ nm$ working on the samples in raster scan exposure mode. One of the most relevant aspect of this apparatus is its exposure speed with respect others maskless techniques, as for example the EBL, or other lithography techniques with any kind of mask. In fact, the nominal $\mu MLA$ exposure speed is 30 $mm^2/min$. On the other hand, the nominal resolution is between 500 and 1000 $nm$, far lower than high-resolution techniques as EBL.

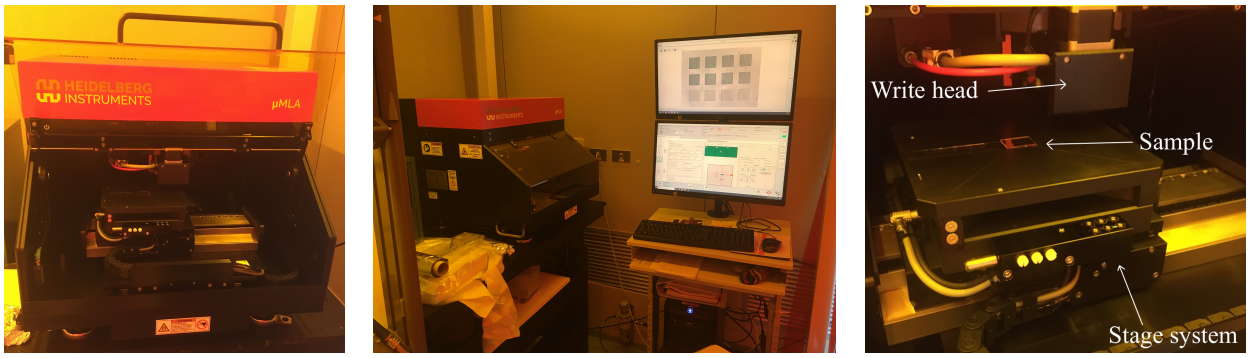


(a) (b) (c)

Figure 1.3: (a) The $\mu$MLA laser writer; (b) Laser writer setup in the clean room; (c) Detail of the $\mu$MLA exposure module.

### Photoresist and developer

The photoresist is a particular type of photosensitive material specifically developed for lithography. There exist two kinds of photosensitive materials suitable for lithography techniques: positive photoresists and negative photoresists. In a positive photoresist the UV light makes the material soluble and after the contact with a dedicated solvent it can be removed simply with water. Conversely, in a negative photoresist the UV light secures the material to the substrate and the non-exposed portion is removed by the solvent in the development stage. The photoresist adopted in this work was the positive photoresist *ma-P 1225G*. It belongs to the series *ma-P 1200G*, designed for grayscale lithography [4]. The *ma-P 1225G*, in particular, is designed for grayscale lithography on height $< 2.5\ \mu m$. Its diffractive index was obtained for $\lambda = 633\ nm$ with a Spectroscopic Ellipsometer VASE (J.A. Woollam). The obtained value is $n = 1.63$. This material is designed to have a more linear response with respect to binary photoresist and shorter exposure time. The specific developer for the *ma-P 1225G* is the *ma-D 532/S*. It is an aqueous-alkaline and surfactant containing Tetramethylammonium Hydroxide (TMAH) based developer. Both resist and developer are produced by *Micro Resist Technology*.

### Spin coater

This instrument is designed to deposite thin layers of resists upon a rigid substrate. The substrate is hold on a rotating platform by a vacuum system activated by the operator. The desired layer thickness depends by the set spinning time and speed. The adopted spin coater is the WS-650MZ-23NPP model made by Laurell Technologies Corporation [11]. This model is able to achive the

[5] Led sources with $\lambda = 390\ nm$ and $\lambda = 365\ nm$.

maximum rotational speed of 12000 rpm. In our work, to obtain a 2.5 $\mu m$ thickness resist layer we set 3 second of acceleration from 0 to 3000 rpm, 30 seconds at the steady rotational speed of 3000 rpm, and 10 seconds of deceleration.

**Hot plate**

Stuart hot plate was used to warm up the samples to perform the so-called "soft-baking" to secure and evaporate any solvent or bubbles in the photoresist before the exposure. We used it also for the post-baking procedure in some samples.

**Profilometer**

The adopted profilometer was the KLA Tencor P-17. For all the samples of this work the profilometer was set with a stylus applied force of 5 $mg$, a scan speed of 20 $\mu m/s$, and a sampling rate of 50 $Hz$.


Figure 1.4: Chimical hood with all the required materials and instruments for the preparation and development of samples.

### 1.3.1 Optical elements fabrication

In this section we will present the general fabrication procedure adopted. The main difficulty for samples fabrication came from the fact that, working on thin resist layers, the order of magnitude regarding the structure reliefs that we were dealing with was comparable to air dust. This is the reason why it was necessary to carry out all the experimental steps of sample preparation, exposure, and development, in a clean room. First of all, we needed to prepare the substrate to deposit on its surface the photoresist layer. Cleaning is a very critical one. A good result depends basically on this preparation. For the same reason, the first step to prepare the sample was a deep cleaning procedure of the glass substrate. The adopted transparent substrate was a microscope glass slide, 1 mm thick, cut to slices of 1 $inch \times 1/2$ $inch$. This step was realized with the use of a 50:50 distilled water/isopropanol solution. After cleaning, the substrate was dried with a gentle flow of nitrogen air. Once the substrate was prepared, the next step was to deposit a 2.5 $\mu m$ photoresist layer upon it. To achieve the formation of a 2.5$\mu m$ thickness layer, we spread 7/10 drops of photoresist on the glass surface making it rotate at 3000 rpm for 30 seconds in the spin coater. A soft-baking process is needed for solvent or bubbles evaporation. This step consists in heating the sample on an electric hot plate at the temperature of 95° $C$ for 60 seconds. At this point the sample is ready for the exposure. After the positioning of the sample on a dedicated platform ad its fixing on that thanks to the activation of a vacuum system, all is ready for the exposure. Initialization process of the $\mu MLA$ consists in a wizard software [7]. The grayscale image of the pattern to replicate on the glass support is made with a specially provided MATLAB script. During the wizard procedure there are a lot of parameters and aspects to set up but the deep study of all the possibilities that $\mu MLA$ offers goes beyond the purpose

of this work. So we considered only the fundamental aspects of this process. At first, we had to set up the size of the substrate and the focusing mode which could be optical or pneumatic. In the case of transparent substrates, the right one is the pneumatic mode. In this way the system is able to focus the laser beam using a blow of compressed air. At this point the wizard proceeds following the steps:

1. Select the grayscale bitmap image representing the pattern;
2. Set the desired value of resolution and $n\_over$. The "n-over" approach is a method to reduce the errors on the edge of the exposing field. Adopting this feature the exposure is performed overlapping the field to mediate the positioning errors on the edges of the exposure field. In this case the $n$ value is the number of times that the $\mu MLA$ overlaps the exposure fields;
3. Convert the image in an apposite file for the $\mu MLA$ firmware;
4. Launch the automatic function to find the sample's center and to focus the writing beam on it;
5. Set the size of area to expose;
6. Set the dose value;
7. Launch the writing procedure;

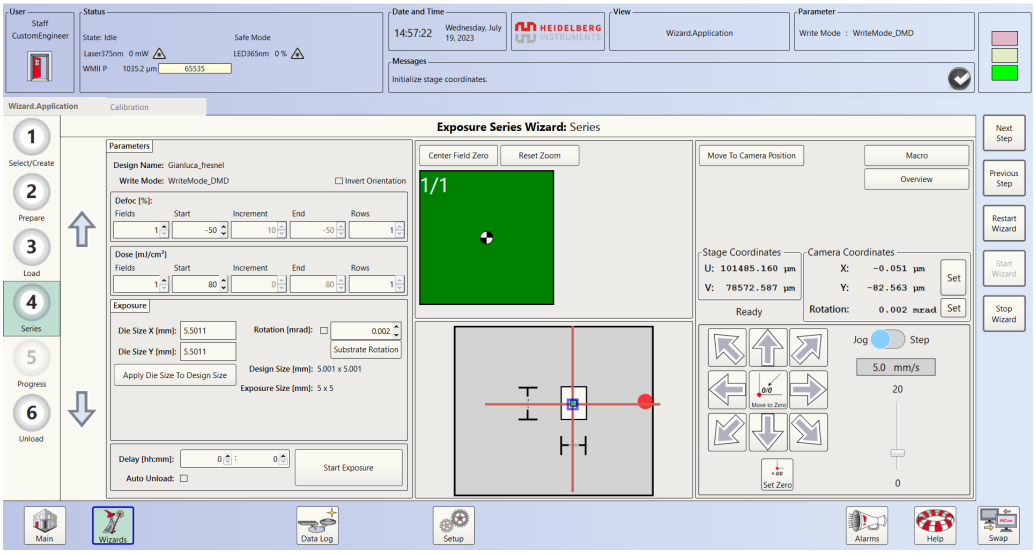


Figure 1.5: in the final step of the wizard procedure we were able to set dose, position and other parameters for a single or a series exposure of the pattern loaded in the previous steps.

After the exposure, it is necessary to proceed with the development. Once released the vacuum system to hold in position the sample during exposure, we deposited on it few drops of not-diluted developer in order to cover the exposed surface. At this point we waited for 1 minute sharp and then immediately we washed the sample with the proper amount of distilled water. At this point it is already possible to distinguish the pattern on the sample surface. After the development procedure the sample fabrication is completed [6]. There are two main elements that could compromise the quality of the produced samples: surface's roughness after the development and the stitching effect. The first aspect was considered in relation to the post baking procedure and so some samples were realized modifying the duration and the presence of this step to observe a possible relation between this element and the surface roughness. The latter is caused by exposure zones positioning errors. This effect is clearly visible in the figure 4.1. Adopting the n-over to reduce the stitching effect is a general method in lithography technique. At first we didn't know if the $\mu MLA$ system adjusted automatically the mean of the dose based on the number of exposure layers set in the n-over parameters during the initialization process. Performing an attempt we observed that the n-over operates correctly with respect to the spatial aspect of the method but the dose is not automatically mediated. For that

[6] We also tried to modify the procedure repeating baking process before the development.

reason, increasing the n-over parameter we obtained an overexposure of the samples at equal dose parameter varying the n-over value. To obtain similar depth profiles of samples with n-over 2 and without n-over the dose has to be set around 4 times grater for the latter case. Adopting the n-over approach, the writing time is increased by a factor $n^2$. This is not a huge problem considering n-over values equals to 2 or 4 given the nominal writing speed of the $\mu MLA$ and the sizes of the samples to expose.

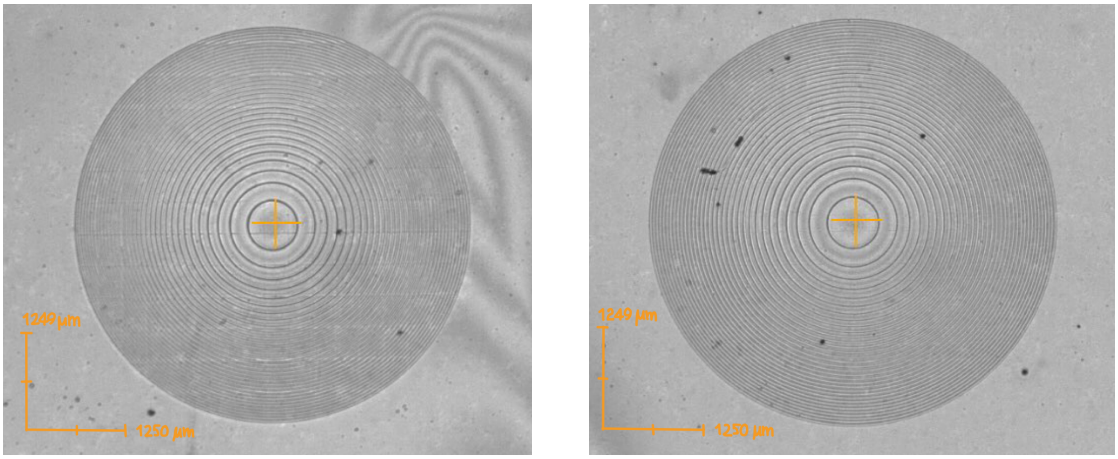


(a) (b)

Figure 1.6: Stitching effect reduction example with two lenses with the same $f = 15cm$. The lens (a) has been obtained without n-over , instead the lens (b) has been obtained with n-over 2.

### 1.3.2 Optical characterization

The design of the realized optical elements is based on the Fourier Optics in the approximation of paraxial wave and in the so-called "far field" or "Fraunhofer regime" [2]. With this approach we were able to describe the effect of an optical element on a normal incident wave and so the resulting image on a screen. In fact, the image on a far screen from the first plane ($z = 0$), is the 2D Fourier Transform of the wave transmitted across the optical element [7] and the intensity pattern is proportional to the square modulus of the complex field:

$$U(x,y) \propto \frac{e^{ikz}}{i\lambda z}\, FT[U^t(\xi,\eta)]\left(\frac{x}{\lambda z}, \frac{y}{\lambda z}\right) \tag{1.2}$$

where the couple of coordinates $(\xi, \eta)$ represents the points on the first plane at $z = 0$, while the couple $(x, y)$ identify the points on the image formation plane. The $\hat{z}$ axis represent the optical axis. So, to perform the calculation of $U(x, y)$ we need to know $U^t(\xi, \eta)$. It is the transmitted field across the optical elements and is given by:

$$U^t(\xi,\eta) = t(\xi,\eta)U^i(\xi,\eta) \tag{1.3}$$

where the $U^i$ is the incident field and $t(\xi, \eta)$ is the transmission function of the optical elements. We considered an incident plane wave and we observed how the optical element deform the wave front. To obtain an incident plane wave on the optic element, we formed a Gaussian beam and set the optical element on its waist.

$$G(x,y,z) = G_0\,\frac{W_0}{W(z)}\,e^{-\left(\frac{x^2+y^2}{W^2(z)}\right)}\,e^{-jkz+j\zeta(z)-jk\frac{x^2+y^2}{2R(z)}} \Rightarrow G(\xi,\eta,0) = G_0\,e^{-\left(\frac{\xi^2+\eta^2}{W_0^2}\right)} = U^i(\xi,\eta) \tag{1.4}$$

[7] Reflected components of the incident wave were ignored.

| | |
|---|---|
| $W_0 = \sqrt{\frac{\lambda z_0}{\pi}}$ | Waist radius |
| $W(z) = W_0\sqrt{1+\left(\frac{z}{z_0}\right)^2}$ | Beam radius |
| $R(z) = z\left(1+\left(\frac{z_0}{z}\right)^2\right)$ | Curvature radius |
| $\zeta(z) = \arctan\frac{z}{z_0}$ | Gouy Phase |

Table 1.1: Gaussian beam parameters

The meaning of the several parameters in the equation (1.4) are reported in table (1.1). As light source we adopted the HNL150L-EC system [10]. It is a He-Ne laser with a nominal wavelenght $\lambda = 632.8\ nm$. To resize the Gaussian beam we used the SLM (Spatial Light Modulator) model PLUTO-VIS-014 (Holoeye) [8]. The adopted camera for data acquisition was the ThorLabs DCC1545M model with a sensor size of 1024 $\times$ 1280 pixels [9]. Each pixel has a nominal side length of 5.2 $\mu m$. After the SLM we positioned along the optical path a beam splitter to redirect half of the beam on a second camera. So we were able to control the input beam and the resulting image at the same time.

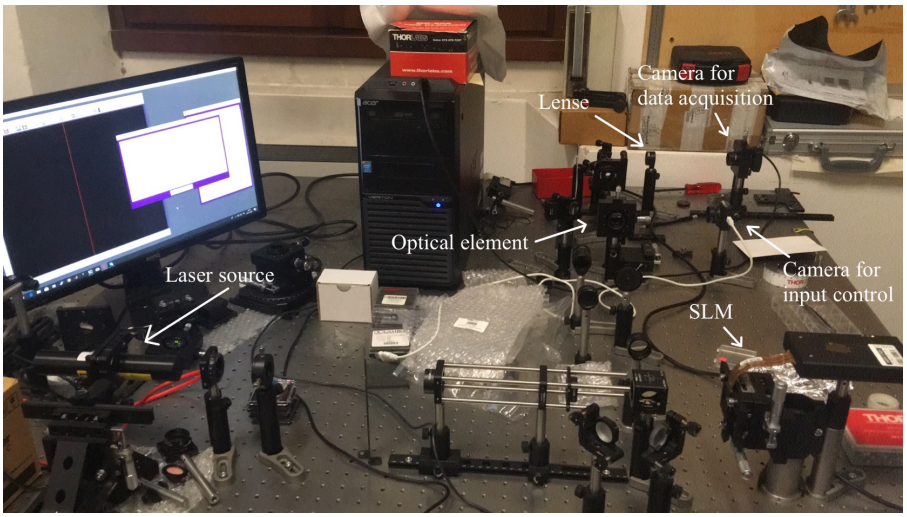


Figure 1.7: Optical bench setup.

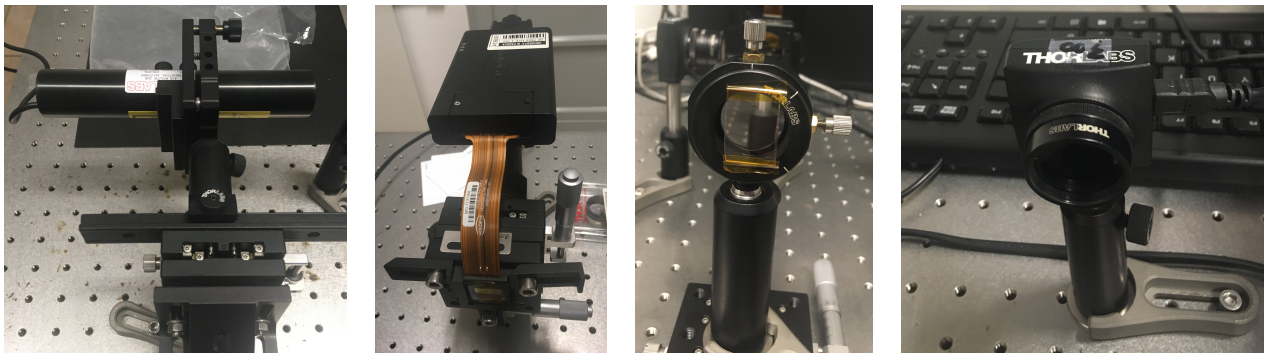

(a) (b) (c) (d)

Figure 1.8: (a) Laser source; (b) SLM for input beam formation; (c)Example of DOE mounted in the optical line;(d) Camera for data acquisition;

# Chapter 2

# Dose Calibration

Before fabricating optical elements we had to know the behavior of the $\mu MLA$ and the main characteristics of the sample that we were going to realize. Therefore, our aim in the first part of the work was to obtain a dose/thickness calibration curve and assess the morphological main characteristics of the samples. To do that we designed and realized several samples of dose matrices changing some design and exposure parameters. In this chapter we will describe in detail this procedure, the measuring process and the results we achieved.

## 2.1 Dose Matrix design and fabrication

A dose matrix is an exposure pattern particularly suitable to study the dose/thickness relation for a fixed level of gray. The matrix that we designed had 8 columns and 7 rows. Each line corresponds to a value of dose set during the initialization procedure of the laser writer. So, what we needed was a bitmap image representing 8 different fields of gray tone placed on column. Such image will be the model of dose matrix column. The bitmap image in the figure 2.1 represents the pattern that we designed. It was generated by a MATLAB macro. Once that bitmap image was selected, we had to set the laser writer to expose 7 identical vertical stripes with different values of dose. Placing side by side 7 columns we obtained the desired matrix structure. We left around every single gray die a side of 60 $\mu m$. The size of each bitmap pixel was set to $5\mu m$. Therefore, the sizes of a single gray square was 500 $\mu m \times 500$ $\mu m$ and it corresponded to 100 pixel. The parameters changed during the fabrication procedure were: the dose intervals and then the dose steps between one column and the following one, n-over values, post-baking duration. Overall we produced the 11 samples listed in the table 2.1.

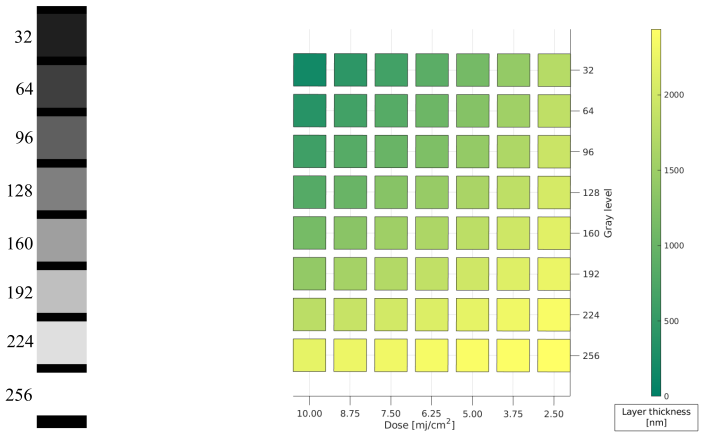


Figure 2.1: The first image is a single column gray-scale pattern, the second one rappresents the mean depth value of the dose matrix 20221102_1 .

| ID | Initial dose ($mJ/cm^2$) | Final dose ($mJ/cm^2$) | Dose step ($mJ/cm^2$) | n-over | Post Baking (sec.) |
|---|---|---|---|---|---|
| 20221017 | 10 | 70 | 10 | / | / |
| 20221018 | 10 | 70 | 10 | / | / |
| 20221021 | 10 | 40 | 5 | / | / |
| 20221028_1a | 10 | 40 | 5 | 2 | / |
| 20221028_1b | 10 | 40 | 5 | / | / |
| 20221028_1c | 10 | 40 | 5 | 4 | / |
| 20221028_2 | 5 | 20 | 2.5 | 2 | / |
| 20221102_1 | 2.5 | 10 | 1.25 | 2 | / |
| 20221102_2 | 2.5 | 10 | 1.25 | 2 | 60 |
| 20221103_1 | 2.5 | 10 | 1.25 | 2 | / |
| 20221103_2 | 2.5 | 10 | 1.25 | 2 | 180 |

Table 2.1: List of samples realized and their main characteristics.

## 2.2 Data analysis

### 2.2.1 Dose curves

To realize the dose curve we measured the depth of each zone with the profilometer. We performed a scan along each row of the matrix. Doing so, we obtained the digging profile of each matrix row. The zones measured correspond to different dose values at constant gray level. The measures so performed correspond to the profile obtained in the figure 2.2. All the profiles measured had an analogous shape. The first observation was that on the sides of each field the steps were very steep. This fact reveals a good precision of the writing system. Particularly at low gray level the surface roughness appears good. At high gray levels it becomes evident the stitching represented by a periodic saw-tooth shape trend. From the profile, using a MATLAB script we were able to calculate the mean depth and its standard deviation field by field. Plotting and fitting the mean depth of each field as a function of the dose values we obtained several dose curves (one for each row of the matrix considered). So we were able to evaluate the linear response of the resist to the dose. The errors associated to the mean depth value were the intervals of standard deviation. From the first samples we started to identify the right dose interval to obtain a linear response and the right depth intervals between 0 and $\sim 1500\mu m$. When we set the n-over value to 2 and 4 for the first time we had an overexposure of the resist and after development we found out that a lot of dies were completely removed. To avoid this situation and considering that we didn't expect evident inhibition at low level of dose [5], we reduced the initial dose and the interval range. So we obtained the first good sample for the analysis, with n-over 2. It was the one named 20221102_1.

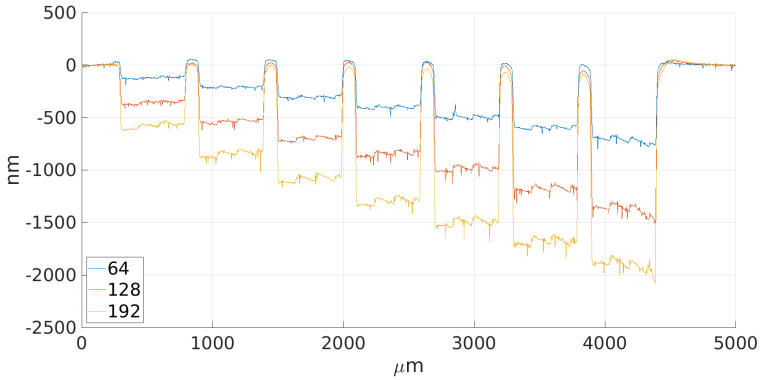


Figure 2.2: Profile of the matrix rows corresponding to the gray value 192, 128, and 32 of the sample 20221102_1 obtained by a profilometer scan.

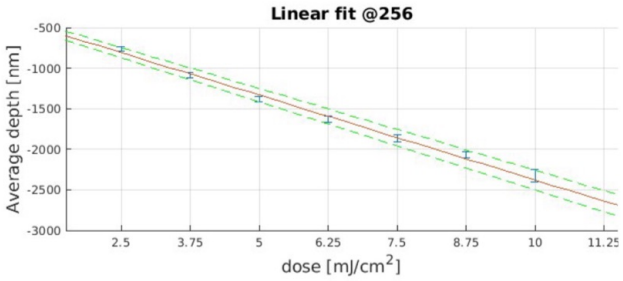
Linear fit @256
Average depth [nm]
dose [mJ/cm$^2$]

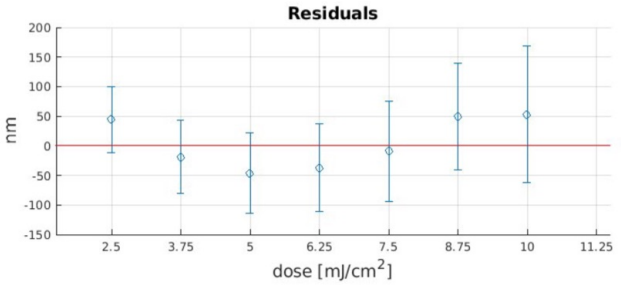
Residuals
nm
dose [mJ/cm$^2$]

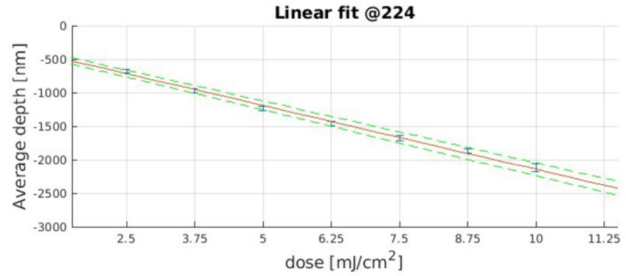
Linear fit @224
Average depth [nm]
dose [mJ/cm$^2$]

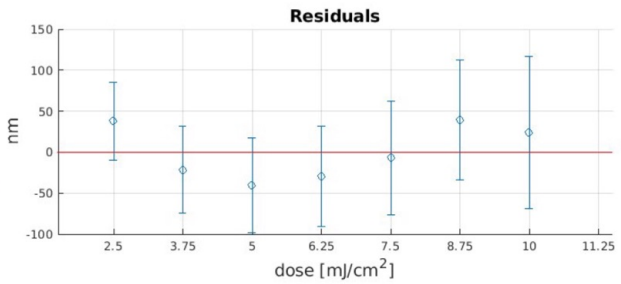
Residuals
nm
dose [mJ/cm$^2$]

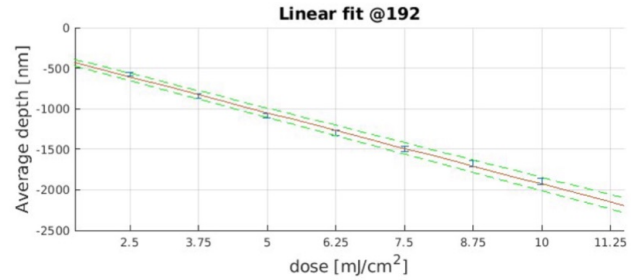
Linear fit @192
Average depth [nm]
dose [mJ/cm$^2$]

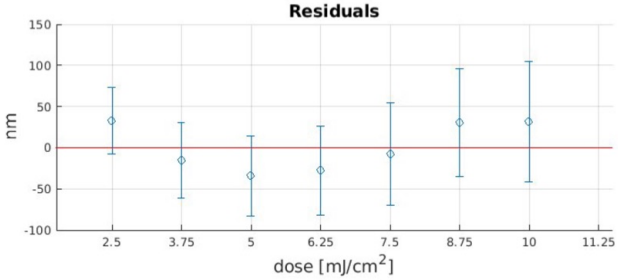
Residuals
nm
dose [mJ/cm$^2$]

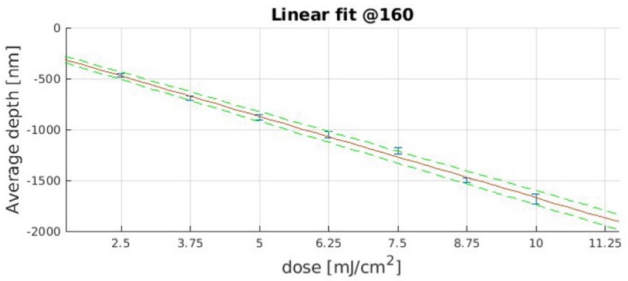
Linear fit @160
Average depth [nm]
dose [mJ/cm$^2$]

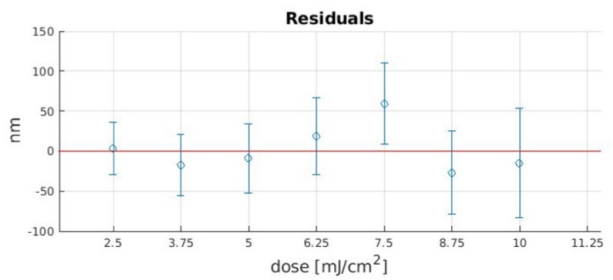
Residuals
nm
dose [mJ/cm$^2$]

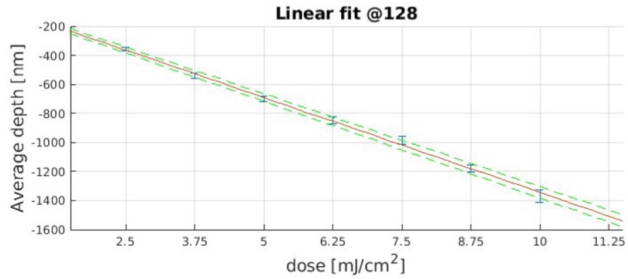
Linear fit @128
Average depth [nm]
dose [mJ/cm$^2$]

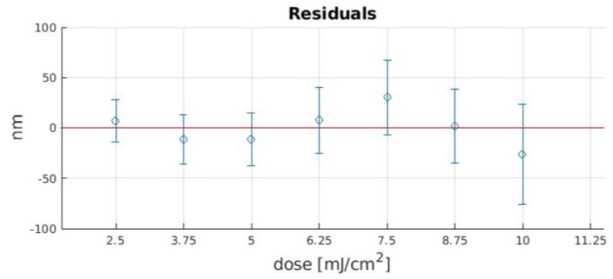
Residuals
nm
dose [mJ/cm$^2$]

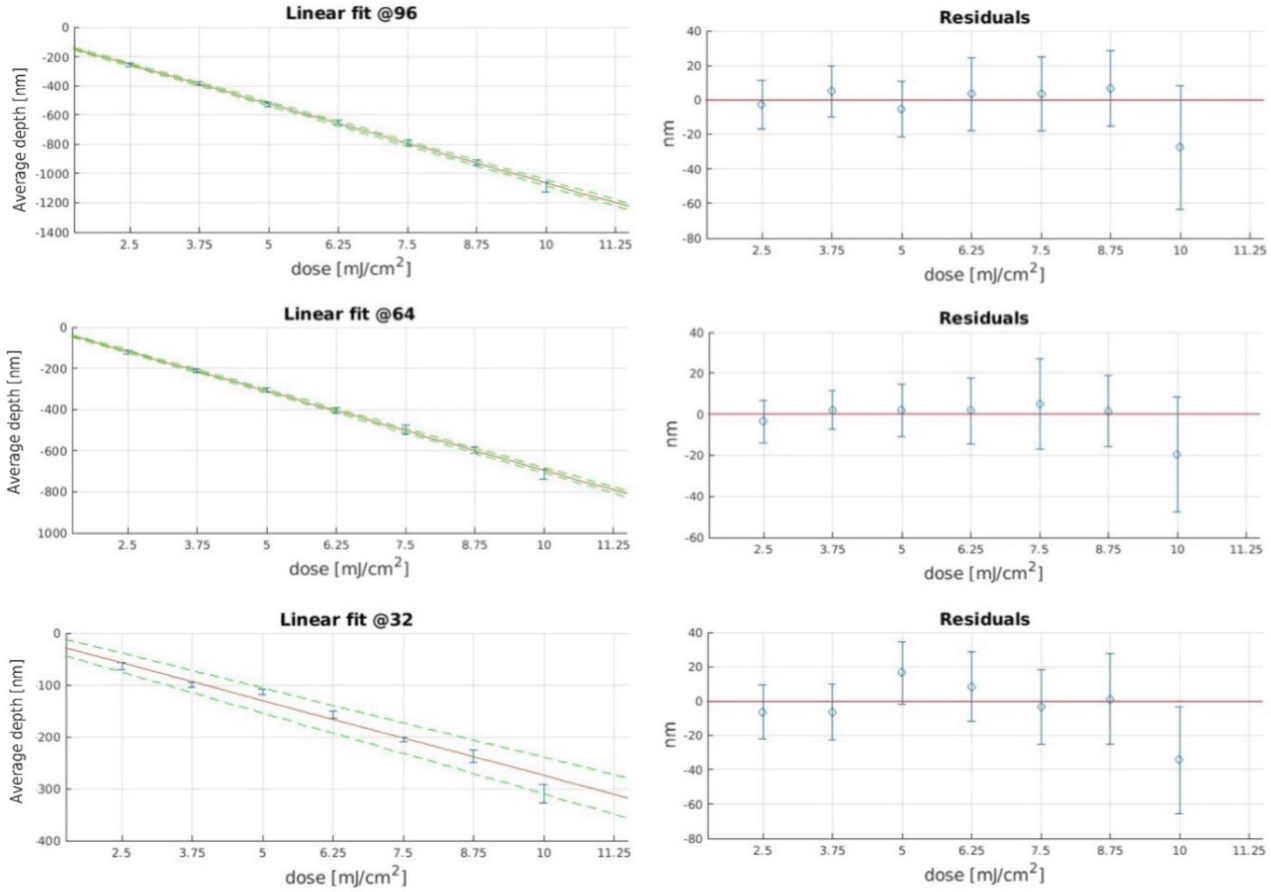


Figure 2.3: Graphs of the linear fits for the dose matrix 20221102_1.

| Gray level | a $(nm)$ | $\sigma_a$ $(nm)$ | b $(10^{-1} \times \frac{mm^3}{J})$ | $\sigma_b$ $(10^{-1} \times \frac{mm^3}{J})$ |
|---|---|---|---|---|
| 256 | -285 | 44 | -209 | 8 |
| 224 | -239 | 36 | -190 | 6 |
| 192 | -168 | 31 | -176 | 5 |
| 160 | -74 | 25 | -160 | 4 |
| 128 | -37 | 14 | -131 | 3 |
| 96 | 18 | 7 | -108 | 1 |
| 64 | 75 | 5 | -77 | 1 |
| 32 | 15 | 13 | -29 | 2 |

Table 2.2: Fit parameters for the dose curves of the 20221102_1 sample.

From the fit graphics we can observe a general good linearity of the data. Despite this, in the curves @256, @224 and @192, we found in the residuals plots a slight parabolic trend that disappears at lower levels of gray. The average depth of the matrix pixels goes from $\sim 50\ nm$ to $\sim 2300\ nm$. For the fabrication of optical elements in our case we need a maximum depth of $\sim 1000\ nm$. So, once verified the linear response of the resist we had to identify the right value of dose to have a maximal depth on the gray scale. To do that it is simply necessary to analyze the depth of the matrix pixels not by rows but by columns. Doing so we found out the right depth range between the dose value of 3.75 $mJ/cm^2$ and 5 $mJ/cm^2$. At these dose values the maximum depth is respectively $\sim 1100\ nm$ and $\sim 1500\ nm$ in the dose matrix profiles. Also observing the data in this way we found out a parabolic trend of the residuals. The selected range is slightly shifted towards greater $d_{max}$ than the reaquired one because

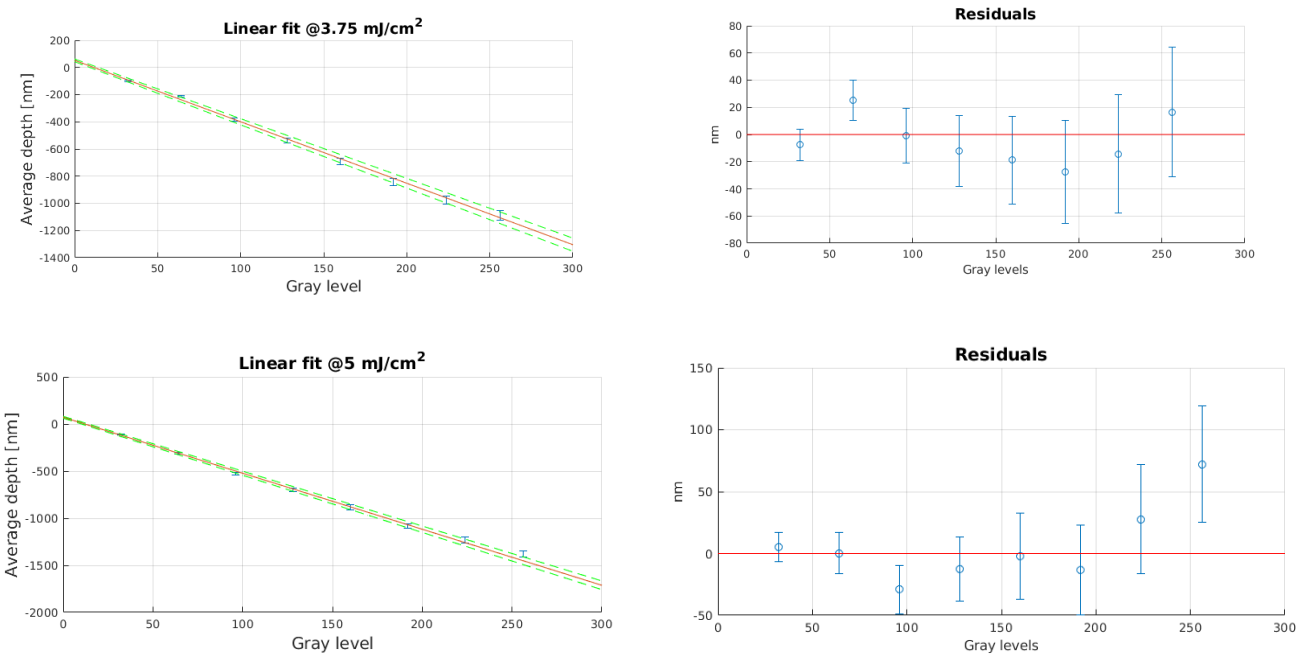


Figure 2.4: Linear fit at fixed dose of the sample 20221102_1.

we expected an overexposition of the samples with more complex pattern to produce. We will see this effect in the following parts of this work regarding the blazed gratings and Fresnel lenses. In the figure (2.5) it is represented as example the 3D matrix obtained. The blocks of the graph represent the resist that remained on the substrate surface of each dose matrix field after the development.

| Dose $mJ/cm^2$ | a $(nm)$ | $\sigma_a$ $(nm)$ | b $(nm/bit)$ | $\sigma_b$ $(nm/bit)$ |
|---|---|---|---|---|
| 3.75 | 52 | 10 | -4.5 | 0.1 |
| 5.00 | 72 | 10 | -5.9 | 0.1 |

Table 2.3: Fit parameters of the graphs in figure 2.4.

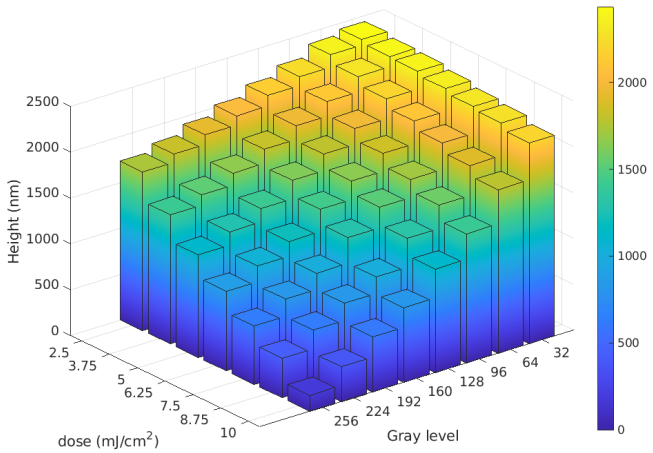


Figure 2.5: Surface of the dose matrix obtained on the sample 20221102_1.

### 2.2.2 Remarks on n-over technique and post-baking

This paragraph has the purpose of providing a qualitative observation about the effects of n-over on the general quality of the samples. Figure 2.6 shows the evident difference between a sample realized with or without n_over. The sample's surface roughness is clearly reduced. However in the n_over sample We can notice periodic spikes generated by the overlap of exposition field to mediate the global exposure desired that is the process of n_over itself. Observing the profile shape of samples realized with and without post backing, in particular 20221103_1 and 20221103_2 or 20221102_1 and 20221102_2, there are no evident improvement in the surface roughness. So there are not strong signals of utility about post-baking procedure at this stage.

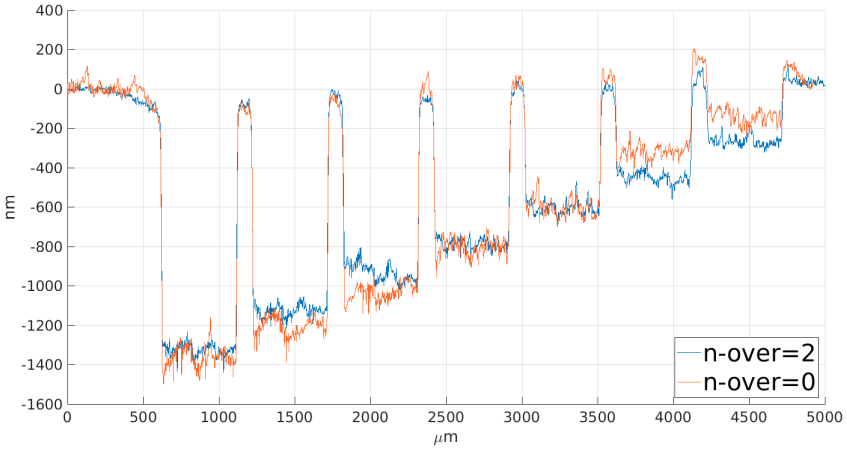


Figure 2.6: Digging profile comparison of samples realized with and without n_over method. In particular the samples considered are the 20221028_1a and 20221028_1b at a gray level 32.

## 2.3 Results

In this first part of the work we tested the maskless lithography gray-scale system. We also observed the linear response of the resist layer exposed on the $\mu MLA$ and we identified the optimal range dose for the fabrication of following optics elements between 3.75 $mJ/cm^2$ and 5 $mJ/cm^2$.

# Chapter 3

# Blazed grating

In this chapter we will present the first optical element realized and tested with the maskless grayscale lithography. The optics fabricated consists in a diffractive version of a prism. The basic idea for the design is what was presented in the first chapter to obtain, from a classical optical element, the equivalent diffractive version.

## 3.1 Design and fabrication

### 3.1.1 Expected behavior of the system

The design of this transmission blazed grating is based on the Fourier Optics in the approximation of paraxial wave and in the so called "Fraunhofer regime". Adopting this condition we could visualize the far-field interference pattern generated by the grating on the back focal plane of a lens [3]. To calculate the expected far-field image under these condition, we need to calculate the transmission function of the grating. To calculate the grating effect we have to quantify the phase shift introduced by the grating considering that the distance traveled across the material $d$ depends by the $\xi$ coordinate of the incidence point. So at the plane described by the equation $z = d_{max}$ the wave traveled a distance equal to $d(\xi)$ in the material and a distance equal to $d_{max} - d(\xi)$ in the air. In particular we find:

$$d(\xi) = \frac{d_{max}}{\Lambda}\,\xi = \frac{\lambda}{\Lambda(n-1)}\,\xi \tag{3.1}$$

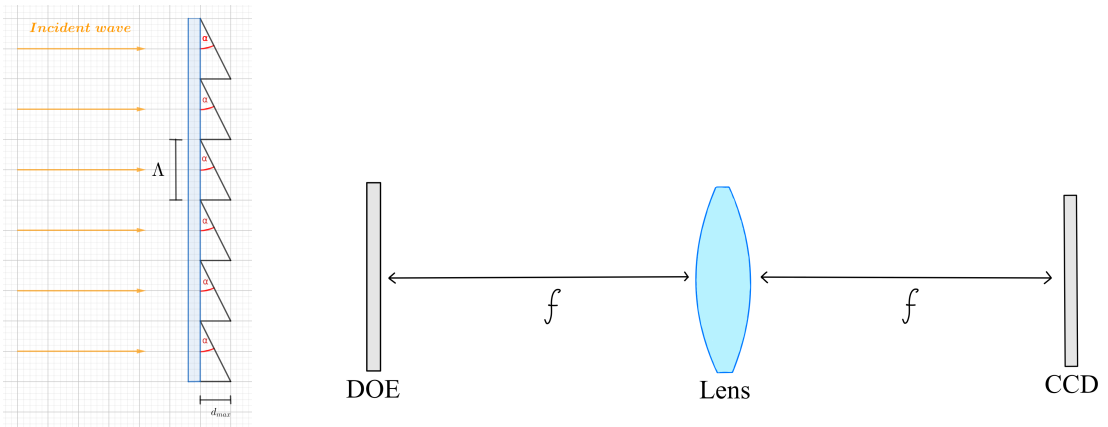


(a) (b)

Figure 3.1: (a)Diffractive version of a prism and its working position. (b)Rappresentation of $f - f$ setup for far-field image formation.

where $\Lambda$ is the grating spatial period in the $\xi$ direction meanwhile its thickness is constant in the perpendicular direction. With this approach we were able to describe the effect of a transmission

grating on a normal incident wave and so the image formation on a far screen. In fact, following this approach, the image on a far screen from the grating's plane ($z = 0$), is the 2D Fourier Transform [2] of the wave transmitted across the grating [1]. So the complex trasmitted amplitude just behind the grating at $z = d_{max}$ is:

$$G^t(\xi, \eta, d_{max}) = G_0^i \; e^{jknd(\xi)} \; e^{jk(d_{max} - d(\xi))} = G_0^i \; e^{jkd(\xi)(n-1)} e^{jkd_{max}} = G_0^i e^{jk\frac{\lambda}{\Lambda}\xi} \; e^{jk\frac{\lambda}{n-1}} \tag{3.2}$$

So the phase shift introduced by the grating deviates the direction of the wavefront propagation[2]. At this point we are able to calculate the far-field image thanks to the expression 1.2:

$$\begin{aligned} U(x) &= \frac{e^{jkz}}{j\lambda z} \iint_{-\infty}^{+\infty} G_0^i \; e^{jkd(\xi)(n-1)} e^{-jk(\frac{x\xi + y\eta}{z})} \; d\xi d\eta = \frac{e^{jkz}}{j\lambda z} \iint_{-\infty}^{+\infty} \; e^{-\frac{\xi^2+\eta^2}{W_0^2}} \; e^{-j\left(k\frac{x}{z} - k\frac{\lambda}{\Lambda}\right)\xi} \; d\xi \\ &\propto \int_{-\infty}^{+\infty} \; e^{-\frac{\xi^2}{W_0^2}} \; e^{-j2\pi\left(\frac{x}{z\lambda} - \frac{1}{\Lambda}\right)\xi} \; d\xi = e^{-(\frac{W_0\pi}{\lambda z})^2 (x - \frac{z\lambda}{\Lambda})^2} \end{aligned} \tag{3.3}$$

So the image in far field that we expected was a gaussian spot with a waist inversely proportional to the input beam waist tilted from the optical axis by the quantity:

$$\Delta x_{exp} = z\frac{\lambda}{\Lambda} \tag{3.4}$$

At this point we had all the elements to design the grating grayscale pattern taking into account the optical bench characteristics at our disposal to test the samples realized.

### 3.1.2 Fabrication parameters definition

In the previous paragraph we showed that the expected image deviation from the optical axis direction is proportional to $z/\Lambda$. To select the grating period we couldn't ignore the testing instruments characteristics. In particular we had to consider the predicted tilt with respect to the camera CCD size. In particular, to avoid a too big tilt value to be visualized on the camera, we had to choose the right value of the focal lens for the optical characterization in the $f - f$ configuration (fig. 3.1,b). Assuming the focal lenght of the lens be $f \simeq 15 \; cm$ we expected the bright spot to be tilted by about 5.2 $mm$ adopting a grating period of 22 $\mu m$. With this choice the tilt value order of magnitude is comparable with the active sensor sizes of the camera. However, since the grayscale pattern was elaborated on multiples of 8 gray levels, we opted for a value of $\Lambda$ multiple of 8. So we set $\Lambda = 24 \; \mu m$ and realized other samples with $\Lambda = 48, 96, 192 \; \mu m$ changing the dose value around the defined one in the calibration phase. At this point, following the same procedure of the dose matrix we realized various samples with the $\mu MLA$ [3].

## 3.2 Data analysis

### 3.2.1 Profile measurement

From a profilometer scan process we obtained an image of the grating profile. From these images we were able to evaluate the sample realized. From the total profiles images of the 24 $\mu m$ period grating, we noticed that it results not as deep as expected. This fact was probably caused by the larger size of the profilometer's tip compared to the small angle on the deepest part of the grating. In general, from the profile images of the samples we could only make indicative observations about the result quality and shapes of the profiles since profilometer capability is not sufficient to always provide a reliable measure due to the samples parameters.

[1] Reflected components of the incident wave were ignored.

[2] Factor $e^{jkd_{max}}$ is a constant phase term that we can ignore.

[3] For all the samples we applied the n_over value equal to 2 and we didn't perform the post-baking.

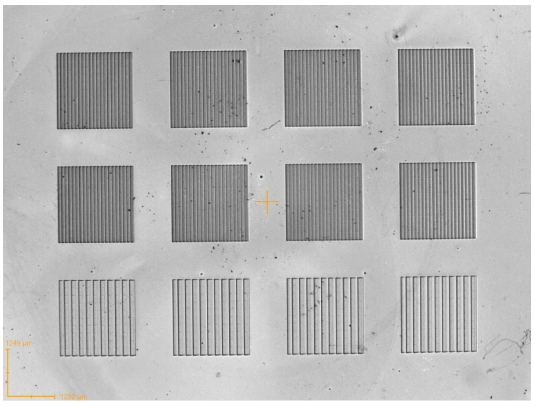

Figure 3.2: Samples named 221111_1,2,3 disposed by row on the same substrate.

| | | | | |
|---|---|---|---|---|
| $\Lambda$ ($\mu$m) | 96 | 96 | 96 | 96 |
| Dose ($mJ/cm^2$) | 3.85 | 3.95 | 4.05 | 4.15 |
| # gray levels | 8 | 8 | 8 | 8 |
| $\Lambda$ ($\mu$m) | 96 | 96 | 96 | 96 |
| Dose ($mJ/cm^2$) | 3.85 | 3.95 | 4.05 | 4.15 |
| # gray levels | 16 | 16 | 16 | 16 |
| $\Lambda$ ($\mu$m) | 192 | 192 | 192 | 192 |
| Dose ($mJ/cm^2$) | 3.85 | 3.95 | 4.05 | 4.15 |
| # gray levels | 16 | 16 | 16 | 16 |

Table 3.1: Table to identify the parameters of the blazed gratings of the image 3.2.

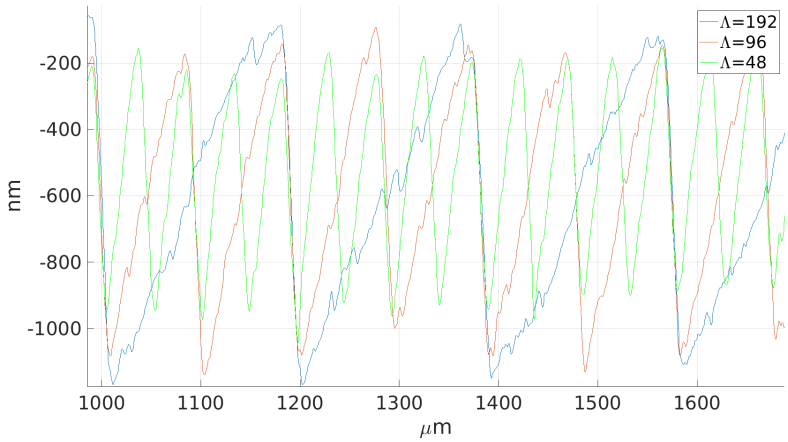


Figure 3.3: Profile shape @$\Lambda = 192, 96, 48$ $\mu m$ and dose value of 3.95 $mJ/cm^2$ from the sample 221111_3.

### 3.2.2 Testing on optical bench

The focal distance of the adopted lens was 20 $cm$. For the sample with $\Lambda = 24\mu$ $m$ we verified that, in these conditions, the tilt was greater than the camera size. So we ignored this sample. Already from the data acquisition process of the other samples we observed the expected behavior of the system. The image is consistent with what we expected and the data profile tells us that the spot is very narrow. The data analysis was developed with the purpose of proving if the spot tilt observed is consistent with the fabrication parameters of the grating and so with its expected value. The single data error (eq. 3.5) was computed considering a background constant contribution evaluated from the mean value of a dark line and a random component evaluated assuming a Poissonian distribution on the single values data, given by $\sqrt{N}$ where N is the integer value from the camera[4].

$$\sigma = \sqrt{\sigma_{bg}^2 + N} \tag{3.5}$$

The distance between the mean of these two spots was taken as the observed tilt. Data analysis and graphical presentation was carried out with MATLAB. To evaluate the spot tilt we performed two different Gaussian fits on the zero order and on the main spot. The first fit was a simple fit ignoring the single data errors. Thanks to this first fit we had the initials parameters to initialize the values for a weighted fit. So the tilt value was computed with the difference between the position of the zero order given by the mean of its Gaussian fit, and the mean of the fit performed on the main spot. The errors on the position of the spots were given by the standard deviation of the Gaussian fits and they was propagated to compute the experimental error on the measure of the tilt:

[4]N=255 corresponds to the maximum luminosity value and N=0 to the minimum

$$\Delta x_{exp} = \mu_{main\ spot} - \mu_{zero\ order} \qquad \sigma_{exp} = \sqrt{\sigma^2_{main\ spot} + \sigma^2_{zero\ order}} \tag{3.6}$$

To the expected value we ascribed the uncertanty value coming from the uncertanty on the $z$ value, that is the error on the distance between the camera and the lens in the experimental setup and its value is $\sigma_z = 1\ mm$. In particular, the expected tilt value is given by the equation 3.4 and the error is given by propagation:

$$\sigma_{tilt} = \frac{\lambda}{\Lambda}\sigma_z \tag{3.7}$$

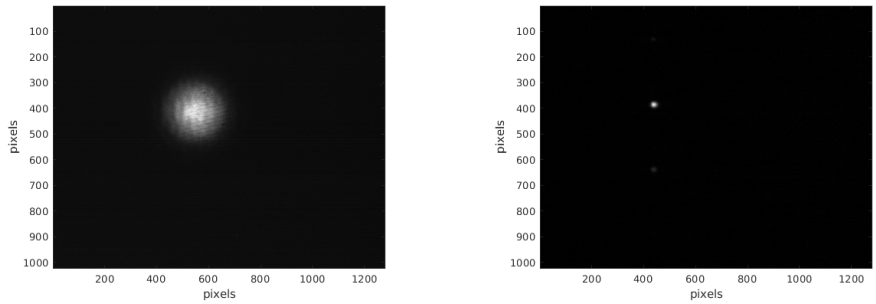


(a) *Gaussian beam* (b) *tilted bright spot*

Figure 3.4: Example of beam used to illuminate the sample and image created in the far-field.

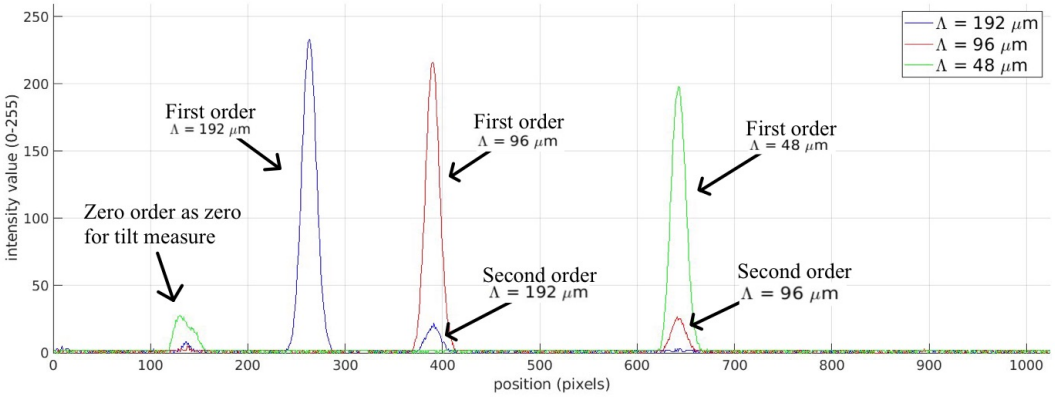


Figure 3.5: Vertical cross-section of the image through the main spot diameter. The others peaks starting from left represents the zero order and the first order of the grating.

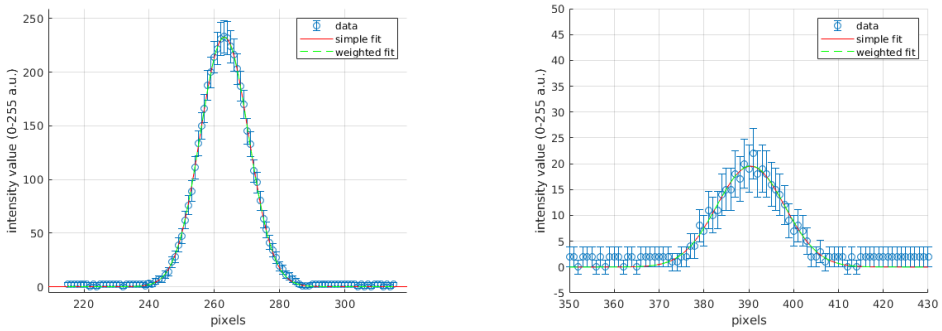


(a) *Tilted spot* (b) *Zero-order spot*

Figure 3.6: Fit performed on the intensity peak to evaluate the main spot deviation.

The compatibility values between the expected position of the spot on the screen and the measured one was computed with the formula 3.8. The values of compatibility minor than 1 indicates an optimal agreement between expected and experimental values.

$$comp = \frac{|\Delta x_{exp} - \Delta x|}{\sqrt{\sigma_{tilt}^2 + \sigma_{exp}^2}} \tag{3.8}$$

| ID | # gray levels | $\Lambda$ ($\mu m$) | Dose ($mJ/cm^2$) | Expected tilt ($\mu m$) | Measured tilt ($\mu m$) | Compatibility |
|---|---|---|---|---|---|---|
| 221110_1 | 256 | 24 | / | / | / | / |
| 221110_2 | 256 | 48 | 3.85 | $2637 \pm 13$ | $2643.3 \pm 1.3$ | 0.50 |
| | | | 3.95 | | $2644.7 \pm 0.4$ | 0.60 |
| | | | 4.05 | | $2636.3 \pm 1.0$ | 0.03 |
| | | | 4.15 | | $2646.3 \pm 1.4$ | 0.73 |
| 221110_3 | 256 | 96 | 3.85 | $1318 \pm 7$ | $1313.5 \pm 0.7$ | 0.73 |
| | | | 3.95 | | $1318.0 \pm 0.6$ | 0.05 |
| | | | 4.05 | | $1318.4 \pm 0.7$ | 0.01 |
| | | | 4.15 | | $1315.4 \pm 0.4$ | 0.45 |
| 221111_1 | 8 | 96 | 3.85 | $1318 \pm 7$ | $1320.8 \pm 1.2$ | 0.37 |
| | | | 3.95 | | $1318.4 \pm 0.9$ | 0.01 |
| | | | 4.05 | | $1315.7 \pm 0.7$ | 0.41 |
| | | | 4.15 | | $1319.0 \pm 0.6$ | 0.10 |
| 221111_2 | 16 | 96 | 3.85 | $1318 \pm 7$ | $1316.8 \pm 0.6$ | 0.98 |
| | | | 3.95 | | $1314.5 \pm 0.8$ | 0.57 |
| | | | 4.05 | | $1318.3 \pm 0.6$ | 0.01 |
| | | | 4.15 | | $1315.6 \pm 0.6$ | 0.42 |
| 221111_3 | 16 | 192 | 3.85 | $659 \pm 3$ | $665.2 \pm 0.9$ | 1.76 |
| | | | 3.95 | | $663.8 \pm 1.1$ | 1.34 |
| | | | 4.05 | | $659.5 \pm 0.9$ | 0.09 |
| | | | 4.15 | | $661.8 \pm 0.8$ | 0.77 |

Table 3.2: Tilt measures and comparison with the expected values.

In addition to what has been observed about the tilt values we noticed an especially good behaviour of the gratings produced with the dose value of 4.05 $mJ/cm^2$. In the specific, in correspondence of this value of dose we noticed the lowest zero-order contribution, denoting a grating profile much closer to the ideal one.

## 3.3 Results

From the analysis it emerges a substantial agreement between the expected and measured tilt values. So we can state that the blazed grating realized works in the expected way. Compatibility values of the experimental and theoretical values underline the good agreement between them, in particular for dose value of 4.05 $mJ/cm^2$. Indeed, the dose affects the zero-order presence and contribution.

# Chapter 4

# Fresnel lenses

In this section we will follow the same scheme of the previous chapter to fabricate another optical element: the Fresnel lens.

## 4.1 Design and fabrication

### 4.1.1 Expected behavior of the system

As we have seen for the blazed grating, to calculated the expected phase pattern we have to find out the transmission function of the lens [2]. To do that we adopted the equation:

$$\begin{aligned} d(\xi,\eta) &= d_{max} - \Big(R - \sqrt{R^2 - \xi^2 + \eta^2}\Big) \\ &= d_{max} - R\Big(1 - \sqrt{1 - \frac{\xi^2+\eta^2}{R^2}}\Big) \\ &\simeq d_{max} - \frac{1}{2}\frac{\xi^2+\eta^2}{R} \end{aligned} \tag{4.1}$$

where $R$ is the curvature radius of the sferical lens. In the last calculation step we applied the Taylor's series expansion at the first order. We can apply this method considering that we are adopting the paraxial approximation. So we can calculate the plano-convex lens transmission function:

$$\begin{aligned} t(\xi,\eta) =&\ \exp\Big[jkn\Big(d_{max} - \frac{1}{2}\frac{\xi^2+\eta^2}{R}\Big)\Big]\exp\Big[jk\Big(\frac{1}{2}\frac{\xi^2+\eta^2}{R}\Big)\Big] \\ =&\ \exp\left[jknd_{max}\right]\exp\Big[-jk\frac{\xi^2+\eta^2}{2R}(n-1)\Big] \\ =&\ \exp\Big[-jk\frac{\xi^2+\eta^2}{2f}\Big] \end{aligned} \tag{4.2}$$

In the last step we neglected the constant phase term and remembered that in the paraxial approximation the focal length of a spherical plano-convex lens is given by the relation $f = R/(n-1)$. So the image at the focal distance is given by:

$$
\begin{aligned}
U(x,y) &= \frac{e^{jkf}e^{jk\frac{x^2+y^2}{2f}}}{j\lambda f}\iint_{-\infty}^{+\infty} G_0^i\ t(\xi,\eta)\ e^{jk\frac{\xi^2+\eta^2}{2f}}\ e^{-jk(\frac{x\xi+y\eta}{f})}\ d\xi\ d\eta \\
&= \frac{e^{jkf}e^{jk\frac{x^2+y^2}{2f}}}{j\lambda f}\iint_{-\infty}^{+\infty} e^{-\frac{\xi^2+\eta^2}{W_0^2}}\ e^{-jk\frac{\xi^2+\eta^2}{2f}}\ e^{jk\frac{\xi^2+\eta^2}{2f}}\ e^{-jk(\frac{x\xi+y\eta}{f})}\ d\xi\ d\eta \\
&= \frac{e^{jkf}e^{jk\frac{x^2+y^2}{2f}}}{j\lambda f}\iint_{-\infty}^{+\infty} e^{-\frac{\xi^2+\eta^2}{W_0^2}}\ e^{-jk(\frac{x\xi+y\eta}{f})}\ d\xi\ d\eta \\
&= \frac{e^{jkf}e^{jk\frac{x^2+y^2}{2f}}}{j\lambda f}\left(\int_{-\infty}^{+\infty} e^{-\frac{\xi^2}{W_0^2}-j2\pi\frac{x}{\lambda f}\xi}\ d\xi\right)\left(\int_{-\infty}^{+\infty} e^{-\frac{\eta^2}{W_0^2}-j2\pi\frac{y}{\lambda f}\eta}\ d\eta\right) \\
&= \frac{e^{jkf}e^{jk\frac{x^2+y^2}{2f}}}{j\lambda f}\ \frac{W_0^2\pi}{2}\ e^{-(x^2+y^2)(\frac{\pi W_0}{\lambda f})^2}
\end{aligned}
\tag{4.3}
$$

and the intensity pattern at the focal distance is:

$$
I(x,y) \propto |U(x,y)|^2 \propto\ e^{-2(x^2+y^2)(\frac{\pi W_0}{\lambda z})^2} \tag{4.4}
$$

So, from the equation 4.4 the image formated at $z = f$ is a very sharp Gaussian spot with waist:

$$
W_0^f = \frac{\lambda f}{\pi W_0} \tag{4.5}
$$

### 4.1.2 Fabrication parameters definition

Thanks to the previous work with the blazed grating we decided to set the dose value at 4.05 $mJ/cm^2$, $n\_over = 2$, and 16 gray levels for the pattern image. In fact, at this condition we had observed good results. The diameter of the lens pattern was 5 $mm$. In this way we were able to illuminate the lens with a radius of $\sim 3$ $mm$ minimizing edge effects. We realized only a sample for this optical element with an array of three lenses with three different focal lengths: 15 $cm$, 20 $cm$ and 25 $cm$.

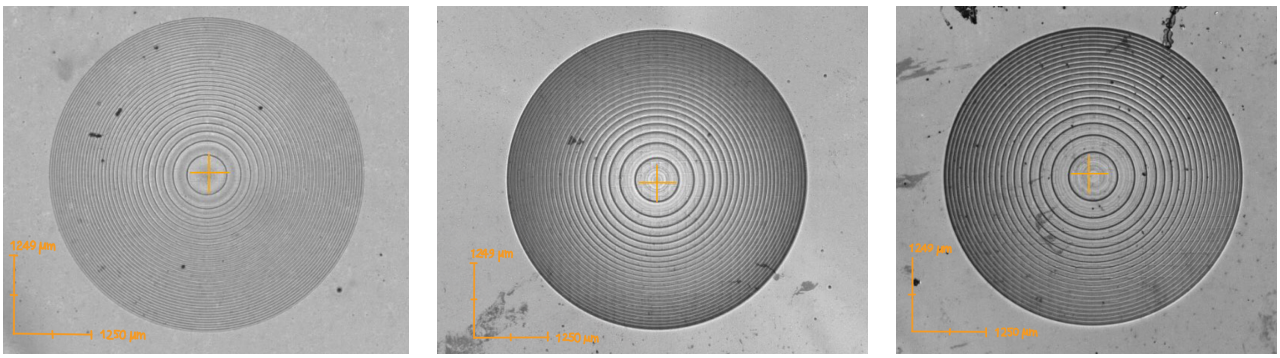

(a) (b) (c)

Figure 4.1: (a)Lens with $f = 15cm$. (b)Lens with $f = 20cm$. (c)Lens with $f = 25cm$.

## 4.2 Data analysis

### 4.2.1 Profile measurement

The profile of the lens was obtained per performing a scan along the diameter with the profilometer. What we can immediately observe from the profile image 4.2 is the reduced sample thickness with respect the expected one, as we observed in the blazed gratin profiles. However the profile shape resembles the designed profile.

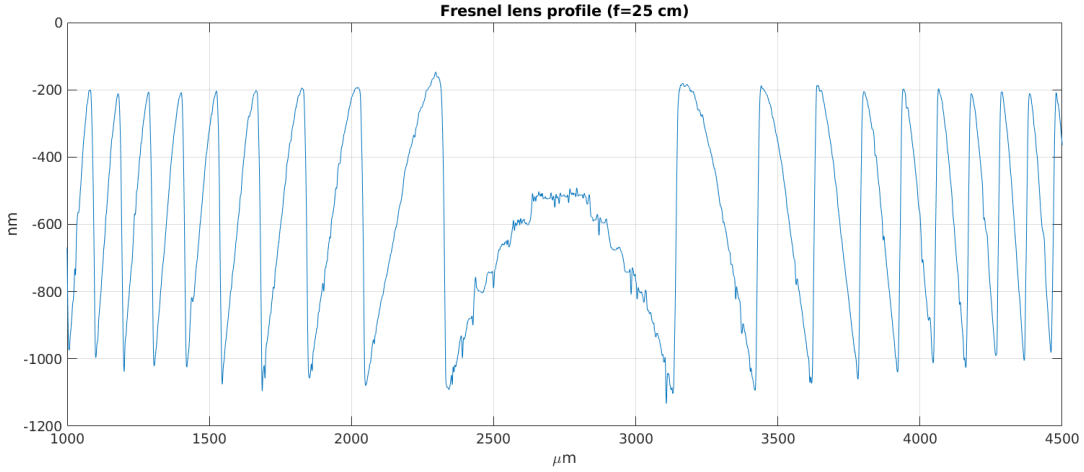


Figure 4.2: Profile of the Fresnel lens with focal lenght $f = 20\ cm$ in the central region.

### 4.2.2 Testing on optical bench

During optical characterization we collected acquisitions of the narrowest spot that we could obtain positioning the camera at the expected focal distance from the lens. Furthermore we collected an acquisition of the incident Gaussian beam. So we had all the data to estimate the input Gaussian beam waist and the focused Gaussian beam waist. As value of waist was assumed the standard deviation of the Gaussian function. To estimate the waist of the input beam we wrote a MATLAB script to find out the average brightest column and row to calculate the center of the beam. On the data of these column and row we performed a weighted fit with a Gaussian function. So we assumed as a good value of input beam waist the weighted mean of the waist of the fits.

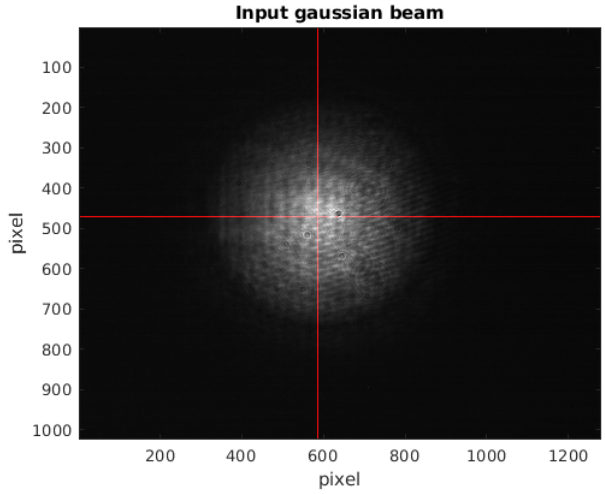


Figure 4.3: Input gaussian beam intensity pattern for lens testing. The red lines indicate the selected line and column of the beam center.

The error on single intensity value was evaluated with the expression 3.5. The final mean value of the waist was $552 \pm 5\ \mu m$. On the image screen, following the same analysis procedure, we analyzed the waist of the spot. From the figure 4.5 is evident the focusing effect of the lens. However, the waist of the Gaussian spot on the focal plane calculated with the equation 4.5 is not compatible with the input beam waist. Probably, the low gain set of the camera needed to observe the high luminosity peak, cut off the tails of the gaussian profile of the data providing a too small estimated value of waist to verify the relation 4.5. For the lenses with $f = 15, 20, 25\ cm$ we measured the waist values of 17, 26, 34 $\mu m$ respectively.

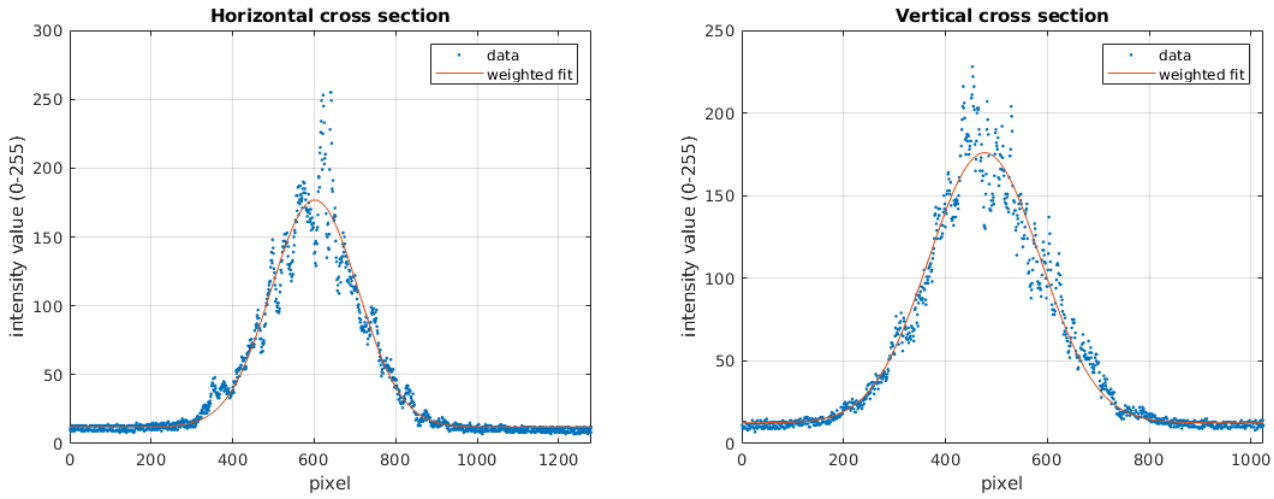


(a) (b)

Figure 4.4: Gaussian fit performed on the vertical and horizontal brightest cross-sections of the input beam.

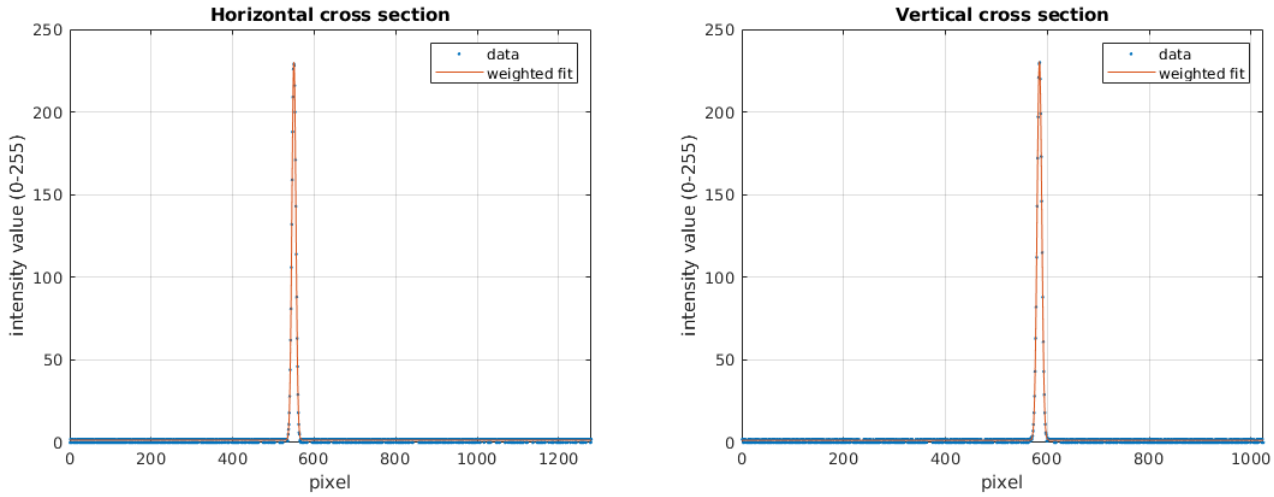


(a) (b)

Figure 4.5: Gaussian fit performed on the vertical and horizontal brightest cross-sections of the image at the focal distance of 25 *cm*.

## 4.3 Results

The fabricated lens profile resembles the designed one and the optical behaviour reproduces what expected from the theory. Despite that, the focused Gaussian spot waist is not compatible with the expected one but we could observe the correct focusing behavior of the lens at the distance equal to the focal length set during the design phase.

# Chapter 5

# Conclusions

In this work we have investigated the design and the experimental procedure to produce three-dimensional optical diffractive elements using maskless optical lithography. In particular, we defined a recipe for the preparation, the exposure and the development of the samples. The initial cleaning procedure, spin-coating and sof-baking provided substrates of sufficient quality for the lithographic process. In the exposure step, considering the main characteristics of the laser writer $\mu MLA$, we concluded that the n-over equal to 2 with a dose of $\sim 4.05\ mJ/cm^2$ are good parameters to realize DOEs with the resist *ma-P 1225G* working with monochromatic light with wavelength $\lambda \sim 630nm$. The observation of the samples profiles produced with the tailored recipe gave the expected profile shape and the behaviours of the Fresnel lenses and blazed gratings were compatible with the ones expected. Despite to reach these results we had to do a lot of work and many attempts to elaborate this procedure, there are still a lot of aspects to investigate. For example, the effects of various levels of n-over and the effects of the post-baking procedure on the final roughness . With respect to bulk optics, a clear advantage of the diffractive optical elements are the extremely high accuracy and low production tolerances, due to the production process: unlike refractive optics, which are typically produced by mechanical procedures of grinding and polishing, DOEs are fabricated by methods similar to those used in the semiconductor industry , thus provide effectively absolute accuracy in feature spacings, which translates to absolute accuracy in angles. Diffractive optical lenses also have functional advantages which can make them very cost-effective when designing an industrial system meant to operate reliably at a high degree of repeatability. Therefore, they can find important applications replacing bulk optics in many fields: beam shaping, optical lithography, microscopy, telecommunications. One of the main limitations of DOEs is that they are designed for a specific wavelength, therefore they suffer from chromatic disperson and they are polarization insensitive [12]. The next step is represented by metasurfaces. In metasurfaces the desired phase pattern is induced by the response of nanostructures on the sample surface. However metasurfaces require high-resolution lithographic technique. In many applications DOE are still a valid compromise in terms of performance and cost.

# Bibliography


[1] Joseph W. Goodman (2005), *Introduction to Fourier Optics*, Roberts & Company Publishers, Englewood (Colorado).

[2] Bahaa E. A. Saleh, Malvin Carl Teich (1991), *Foundamentals of Photonics*, John Wiley & Sons, New York City (New York).

[3] George O. Reynolds, John B. DeVelis, George B.Parrent, Brian J. Thompson (1990), *Physical Optics Notebook: Tuotorial in Fourier Optics*, SPIE Optical Engineering Press, New York City (New York).

[4] micro resist technology GmbhH, *ma-P 1200G — Positive Greyscale Photoresist Series*, micro resist technology GmbhH, Berlin (Germany).

[5] C. Schuster, A. Voigt, G. Grützner, *Grayscale positive photoresist*, The Lithographer (#1, January 2020).

[6] Heidelberg Instruments, *$\mu$MLA technical datasheet*(June 2021).

[7] Heidelberg Instruments, *$\mu$MLA Operator's Guide*(June 2021).

[8] HOLOEYE Photonics AG, *Pluto, Phase Only Spatial Light Modulators (Device Operating Instruction, SLM Software Instructions)*(November 2017, v3.4).

[9] Thorlabs Scientific Imaging, *DCx Camera Functional Description and SDK Manual* (July 2018, v4.82).

[10] Thorlabs Scientific Imaging, *HNL Series Red HeNe Lasers, User Guide* (August 2018, Rev B).

[11] Laurell Technologies Corporation, *Laurell Technologies Operations Manual WS-650 Series* (October 2011).

[12] Engelberg J., Levy U., *The advantages of metalenses over diffractive lenses.* Nat Commun 11, 1991 (2020).